ACS Photonics

pubs.acs.org/journal/apchd5

Letter

Broadband Terahertz Silicon Membrane Metasurface Absorber

Yuwei Huang, Kelson Kaj, Chunxu Chen, Zhiwei Yang, Sheikh Rubaiat Ul Haque, Yuan Zhang, Xiaoguang Zhao, Richard D. Averitt,* and Xin Zhang*

Cite This: *ACS Photonics* 2022, 9, 1150–1156

Read Online

ACCESS | Metrics & More | Article Recommendations | Supporting Information

ABSTRACT: Metasurface absorbers are of particular interest in numerous photonic applications including detectors, photovoltaic cells, and emissivity coatings. We introduce a thin membrane silicon metasurface absorber with periodic elliptical holes that, as demonstrated theoretically and experimentally, achieves very high absorption (≥90%) over a ∼500 GHz bandwidth at normal incidence. Based on the analysis of the effective medium theory, the broadband absorption is attributed to proximal electric and magnetic dipole resonances. The absorption amplitude can also be tuned by ∼20% with above-gap photoexcitation. Due to the unit cell geometry, the carrier density on the top surface and sidewalls of the membrane must be taken into account. Our dynamic membrane silicon metasurface absorber is notably thin and CMOS-compatible, providing a promising platform to realize compact terahertz devices including detectors, modulators, and switches.

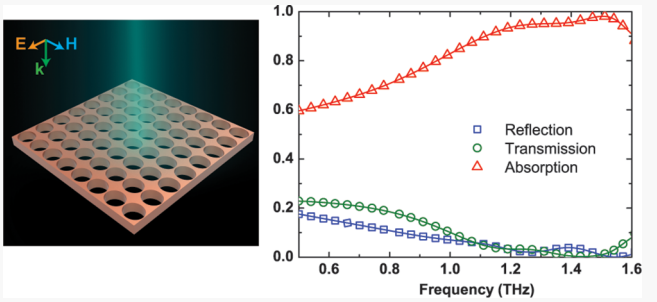

KEYWORDS: *THz metasurface, absorber, membrane, broadband, modulation*

INTRODUCTION

The terahertz frequency regime, lying between microwave and mid-infrared frequencies, has captured the attention of scientists and engineers due to its rich scientific potential.[1−3] Technological advances related to THz waves are not only driven by high-efficiency sources, but also by a variety of high-quality functional devices, including waveplates, beam splitters, lenses, reflectors, and absorbers.[4−8] In recent years, metasurfaces have become a hotspot for effectively manipulating waves from microwave through visible frequencies.[9−11] The ultrathin nature of metasurfaces, relative ease of fabrication, and subwavelength resolution offer considerable potential for THz device miniaturization and system integration.

Metasurface absorbers in particular have attracted great interest due to a host of possible applications, ranging from thermal imaging to energy harvesting.[12−19] Dielectric metasurfaces (including absorbers) complement traditional metallic-based metasurfaces with advantages that include low ohmic loss, temperature stability, and compatibility with CMOS processing.[8,20−25] In addition, dielectric metasurfaces are able to realize not only electric dipole resonances, but also magnetic dipole resonances, providing flexibility to achieve functionalities that are difficult to achieve by metallic-based metasurfaces (for a given polarization), such as electromagnetically induced transparency[26−28] and a higher quality factor,[29−31] among others.

Dielectric metasurfaces are typically composed of high-index dielectric resonators integrated on low-index substrates (e.g., silicon nanodisks on a quartz substrate).[24,26,32,33] Unfortunately, the thickness of the substrate is usually comparable to the wavelength of interest at terahertz frequencies, introducing interference effects. Moreover, the electromagnetic response can be affected by the dielectric contrast between the resonators and the substrate.[34]

Recently, a new type of dielectric metasurface has been developed, consisting of a single layer of high-index material with an array of elliptical holes (e.g., Figure 1a).[35−38] Although such a structure resembles a photonic crystal, the functionality of a membrane metasurface derives from local Mie-type resonances rather than Bragg scattering.[39] More importantly, this membrane metasurface typically has a thickness below 100 μm, making it a strong candidate for device miniaturization. Researchers have proposed using such metasurface dielectric aperture arrays (MDAA) as multifunctional devices including phase gradient structures for wavefront engineering.[35] However, the design of terahertz MDAA absorbers has as of yet not been investigated.

Previous efforts have been made to expand the bandwidth of a metasurface absorber,[8,40−42] typically by using several resonators with different dimensions within a unit cell so that each resonator achieves high absorption at a well-defined center frequency.[27] Another mechanism uses a high-index

Received: January 27, 2022
Published: April 5, 2022

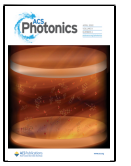

https://doi.org/10.1021/acsphotonics.2c00166
ACS Photonics 2022, 9, 1150−1156

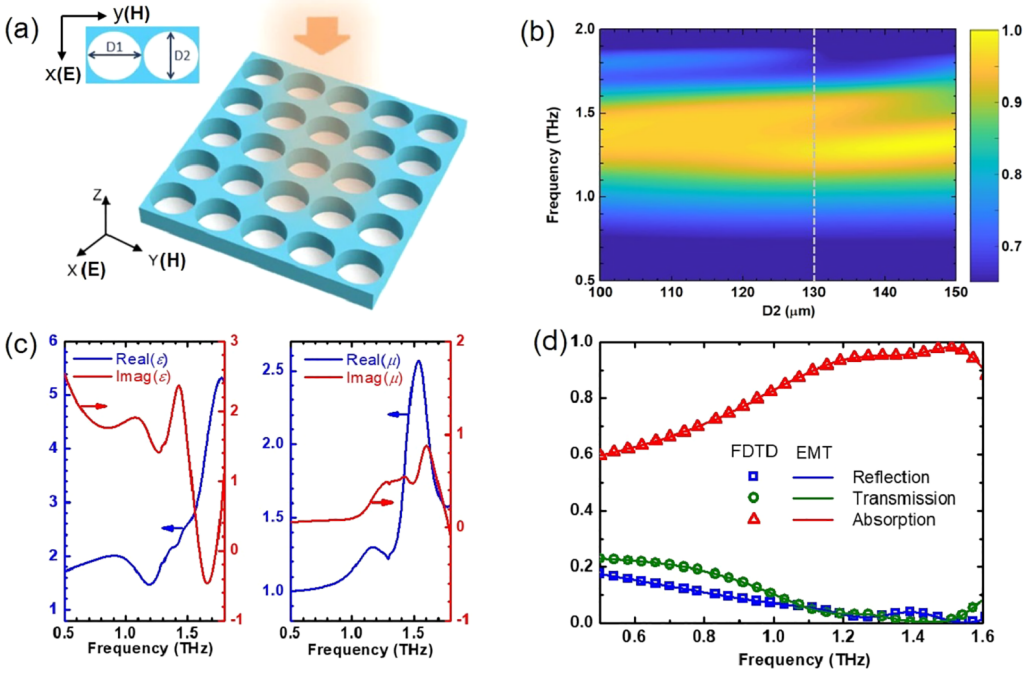

Figure 1. (a) Schematic of the broadband THz silicon membrane metasurface absorber (SMMA). The periodicity is 160 μm and the membrane thickness is 75 μm. (b) Absorption amplitude profile of the SMMA at D_1 = 150 μm with varying dimension D_2 from 100 to 150 μm. (c) Effective permittivity and permeability extracted from SMMA simulations. (c, d) FDTD simulated reflection (blue), transmission (green) and absorption (red) of SMMA (symbols) and calculated spectra (solid lines) using effective parameters in (c).

substrate to increase the internal reflection and trap the wave to achieve broadband absorption.[42] None of these designs have been able to achieve broadband terahertz absorption based on a single pattern on a thin membrane material.

In this paper, a silicon membrane metasurface absorber (SMMA) with an elliptical hole array perforated into a 75 μm thick silicon layer is presented. The metasurface absorber can reach very high absorption (≥90%) over a broad bandwidth (1.1−1.6 THz) at normal incidence. The absorber maintains a relatively broad absorption bandwidth over a large range of incident angles. To understand the broadband absorption theoretically, we used effective medium theory (EMT) and performed mode analysis on the SMMA. In addition, we demonstrate that photogeneration of carriers tunes the absorption amplitude of the SMMA. Simulations reveal that the photoexcitation of both the top layer of the membrane and the sidewall of the elliptical holes must be taken into account to obtain agreement with the experimental results. Our work highlights the effectiveness of SMMAs to achieve broadband terahertz absorption with potential for applications in CMOS-compatible THz systems and for future device miniaturization.

RESULTS AND DISCUSSION

Design and Simulation. The SMMA design is illustrated in Figure 1a with a n-doped silicon membrane suspended in air and perforated with elliptical holes. The doping is approximately 3×10^{16} cm^{-3}. The periodicity of the unit cell is 160 μm, and the overall membrane thickness is 75 μm. In order to optimize the broadband absorption, finite difference time domain (FDTD) simulations were performed with a parameter sweep of D_2 (minor axis of the ellipse) from 100 to 150 μm, while D_1 (major axis of the ellipse) was fixed at 150 μm, as shown in Figure 1b. Detailed analysis of an absorber with D_2 = 130 μm was performed because it showed the largest bandwidth of near-perfect absorption. Simulated reflection, transmission, and absorption spectra of the SMMA are shown as hollow symbols in Figure 1d. For the simulations, the permittivity of the silicon was modeled using a Drude response, with the polarization of the incident terahertz pulse along the minor axis of the ellipse, as shown in Figure 1a. Details of the simulation can be found in the Experimental Section. The simulation results indicate that ≥90% absorption starts at 1.1 THz and remains near unity up to 1.6 THz at normal incidence, corresponding to a bandwidth of 500 GHz. Although the doping concentration is relatively high for the silicon layer, the dielectric loss is still comparable to other dielectric metasurface absorbers in the near unity perfect absorption regime (as shown in the Supporting Information).

To better understand the origin of the broadband absorption in the SMMA structure, the effective permittivity and permeability were retrieved from the simulated transmission and reflection spectra. Based on the transfer matrix method,[43,44] the reflection coefficient r^* and transmission coefficient t^* at normal incidence are

$$r^* = \frac{R^*(1 - e^{i2n^*dk_0})}{1 - R^{*2}e^{i2n^*dk_0}} \quad (1)$$

$$t^* = \frac{(1 - R^*)e^{in^*dk_0}}{1 - R^{*2}e^{i2n^*dk_0}} \quad (2)$$

where $R^* = (z^* - 1)/(z^* + 1)$, z^* is the complex impedance, n^* is the refractive index, d is the membrane thickness, and k_0 is the wavenumber in free space. In order to retrieve z^* and n^* to obtain the effective permittivity and permeability, we use:

https://doi.org/10.1021/acsphotonics.2c00166
ACS Photonics 2022, 9, 1150−1156

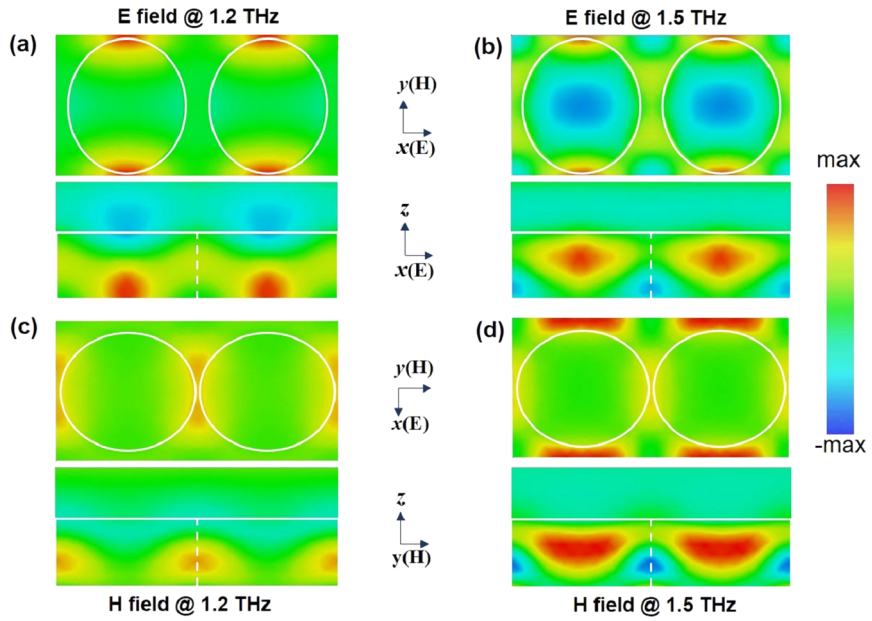

Figure 2. x-Component of the electric field (a, b) and the y-component of the magnetic field (c, d) at f_1 = 1.2 THz and f_2 = 1.5 THz: (a, c) Field distributions at 1.2 THz; (b, d) Field distributions at 1.5 THz.

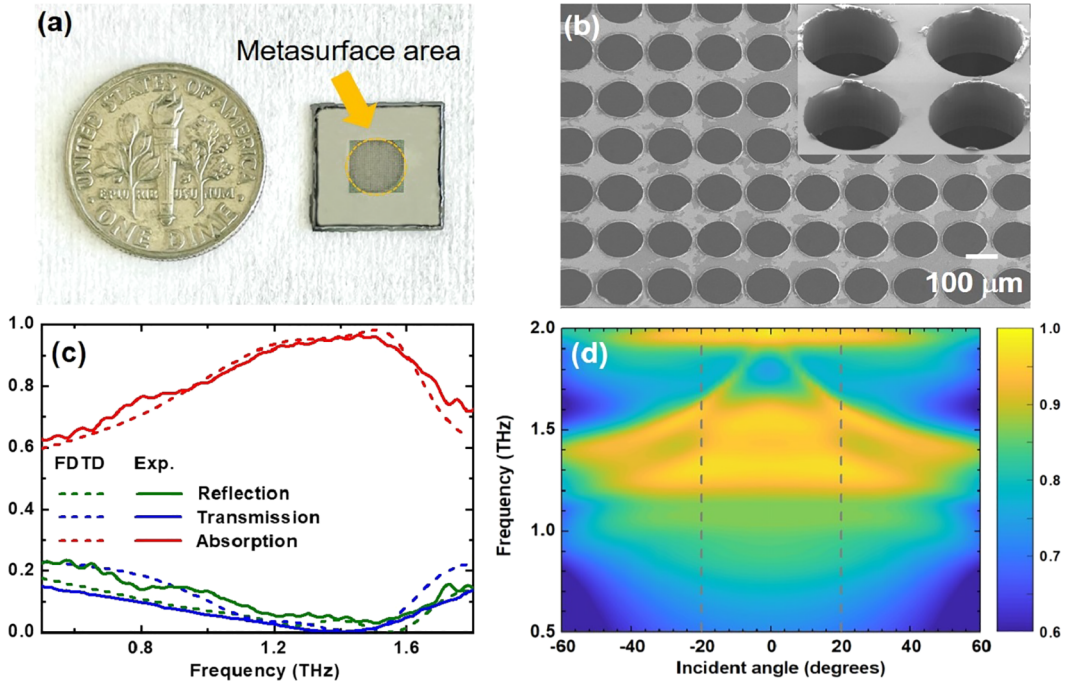

Figure 3. (a) Image of the SMMA sample and (b) scanning electron microscope (SEM) image of the SMMA structure. (c) Comparison of reflection, transmission, and absorption spectra from FDTD simulation and experiment. (d) Dependence of absorption spectrum on incident angle. Gray dashed lines in (d) showed the broadband absorption can be achieved even when the incident angle increases to 20°.

$$Z^* = \pm\sqrt{\frac{(1+r^*)^2 - t^{*2}}{(1+r^*)^2 - t^{*2}}} \tag{3}$$

$$n^* = \frac{1}{k_0 d}\left(-i \ln \frac{t^*}{1 - R^* r^*} + 2m\pi\right) \tag{4}$$

where m is an integer. The permittivity ε^* and permeability μ^* are acquired from $\varepsilon^* = z^*/n^*$ and $\mu^* = z^* n^*$. The retrieved ε^* and μ^* are separated into their real parts (ε' and μ') and imaginary parts (ε'' and μ''), which are shown in Figure 1c.

To validate the retrieved parameters, we used ε^* and μ^* in Figure 1c to simulate a homogeneous slab with the same thickness. The resulting transmission, reflection, and absorption spectra are shown as the solid lines in Figure 1d. The results agree quite well with the FDTD simulations, as shown by the hollow symbols in Figure 1d. In the permittivity spectra, there are two distinct peaks in ε'' at ~1.1 THz and ~1.4 THz, while ε' stays relatively low (compared to bare silicon) below 1.6 THz. Comparatively, μ' remains around 1 below 1 THz, increasing to reach its peak at around 1.5 THz, while μ'' increases from ~0.05 to 0.5 at 1.2 THz and reaches its peak at

https://doi.org/10.1021/acsphotonics.2c00166
ACS Photonics 2022, 9, 1150−1156

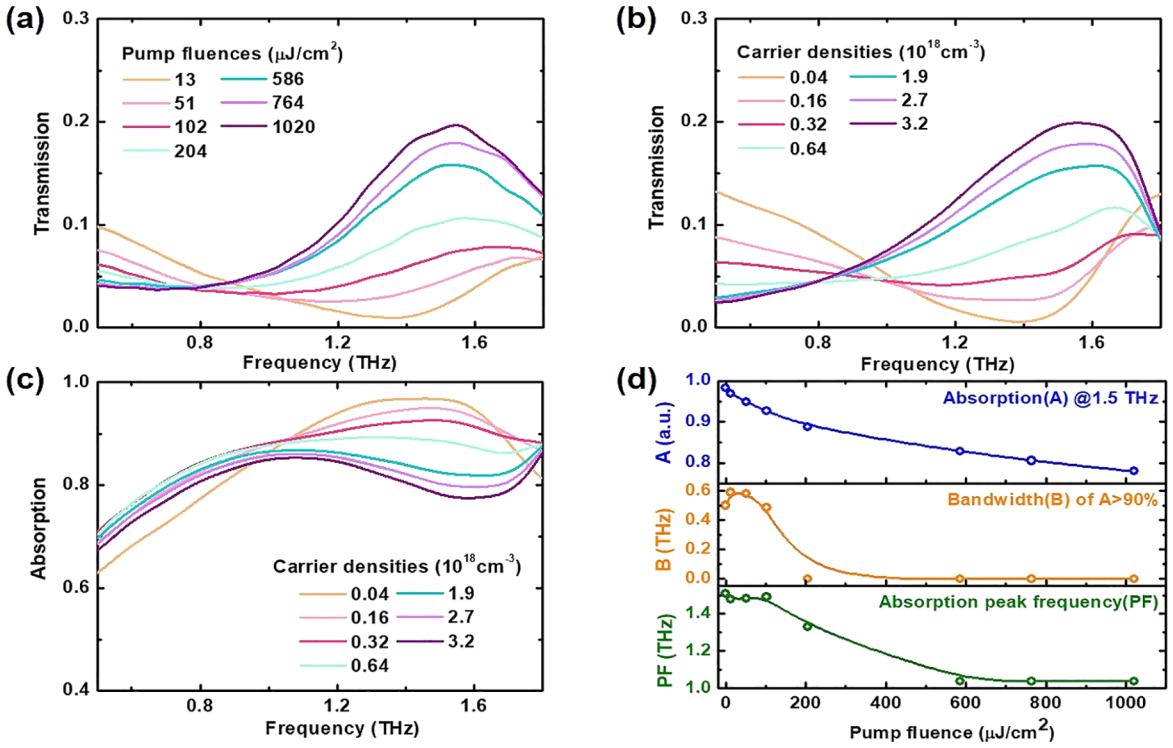

Figure 4. (a) Experimental transmission spectra of the SMMA under different optical pump fluences. (b) Simulation results of transmission and (c) absorption for various carrier densities within 10 μm of the thick top layer and sidewall layer. (d) The absorption at 1.5 THz, bandwidth with absorption ≥90%, and the absorption peak frequency as a function of pump fluence.

around 1.6 THz. The combined effect of ε and μ results in impedance matching between ∼1.2 to 1.5 THz, as required for broadband absorption (i.e., minimizing the reflection) in our membrane metasurface. In order to better understand the broadband absorption, we plotted the electric and magnetic field distribution at the frequencies of the highest absorption amplitudes, that is, at 1.2 and 1.5 THz, as shown in Figure 2.

The x-component of the electric field and the y-component of the magnetic field at 1.2 and 1.5 THz are shown in Figure 2a, c and b, d, respectively. Each figure contains two views where the upper portion is the top view for the $x-y$ plane and the lower portion is the side view of the xz (yz) plane for the electric (magnetic) field. The figures for the side views are chosen at the y (x) position, where the electric (magnetic) field amplitude is the highest. For example, the bottom figures in Figure 2a,b are at the y position in the middle in-between the nearby unit cell. At 1.2 THz, the transverse electric (TE) mode is dominant between nearby unit cells along the x-axis, while no distinct transverse magnetic (TM) mode is observed, as shown in Figure 2a,c. However, at 1.5 THz, there are concentrated electric and magnetic fields between the unit cells along the x-axis and y-axis, respectively (Figure 2b,d). This indicates hybrid resonances comprised of TE and TM modes. The hybrid modes are also consistent with a higher absorption at 1.5 THz than at 1.2 THz.

Experimental Results. We fabricated a SMMA sample to validate and compare with the simulated electromagnetic response using bulk micromachining with fabrication comprised of photolithography, reactive ion etching (RIE), and deep reactive ion etching (DRIE) on a silicon-on-insulator (SOI) wafer. Figure 3a,b shows the images of the SMMA sample. The electromagnetic response was measured using terahertz time domain spectroscopy (THz-TDS) in transmission and reflection. Detailed fabrication processes and measurements can be found in the Experimental Section. The fabrication flow is also included in the Supporting Information. As shown in Figure 3c, the experimental spectra are in good agreement with the simulations. The mismatch between the simulations and experimental results can primarily be ascribed to fabrication limitations and imperfections. As shown in Figure 3b, there is residue on the surface of the sample, which could cause scattering, leading to slight differences with simulation. Overall, the fabricated sample achieves a relatively flat absorption (≥90%) between 1.1 and 1.6 THz. In addition, we also simulated the THz response at different incident angles, as shown in Figure 3d. The results indicate that the bandwidth of absorption ≥90% is relatively constant when the incident angle is below 20° and high absorption (≥85%) can still be achieved over 300 GHz even when the incident angle increases to 40°.

Subsequent to characterizing the static electromagnetic response of the SMMA, optical-pump THz-probe spectroscopy (OPTP) was used to investigate the dynamic response where photoexcitation is used to generate carriers in the silicon. The pump beam consisted of ∼40 fs 800 nm near-infrared (NIR) pulses. Both the pump beam and THz probe beam were at near-normal incidence. Figure 4a shows the transmission spectra of the SMMA for pump fluences ranging from 13 to 1020 μJ/cm^2, corresponding to carrier densities from 0.04 to 3.2× 10^{18} cm^{-3}. As the pump fluence increases, the transmission at ∼1.5 THz continuously increases and reaches ∼0.2 for 1020 μJ/cm^2, while it decreases from 0.1 to 0.04 below 0.8 THz. The observed increase in transmission corresponds to a decrease in absorption.

In order to understand absorption decrease due to carrier photoexcitation, simulations were performed. It was not

https://doi.org/10.1021/acsphotonics.2c00166
ACS Photonics 2022, 9, 1150−1156

possible to reproduce the experimental results by modeling the photoexcitation as a homogeneous increase in the carrier densities for the front surface of the SMMA. For these simulations, the penetration depth of silicon (10 μm for 800 nm excitation) was used and the carrier densities used in the simulation are consistent with published papers.[42,45] However, the simulation results fail to reproduce both the changes in transmission amplitude at ∼1.5 THz and the decreasing trend above 1.6 THz (see Supporting Information). Therefore, the effect of carrier excitation on the sidewalls of the elliptical holes cannot be ignored. As shown in Figure 1a, the primary difference between the SMMA structure from typical dielectric metasurfaces is that most of the silicon has been etched away and the thickness of the sidewall for this structure is comparable to the penetration depth. Additionally, although the pump in the OPTP experiment is at normal incidence, diffraction of the pump on the edge of the holes can result in photocarrier excitation of the sidewalls. Therefore, the sidewall excitation could play an important role. Moreover, since sidewall excitation occurs through diffraction, it is expected that the photoexcited carrier density would be less than for the front surface. Figure 4b shows the simulation results when a photoinduced increase of the carrier density on the sidewall is taken into account. The sidewall carrier densities are approximately 8−40× smaller than the carrier densities on the front under different optical fluences. Detailed parameters are included in the Supporting Information. Using this additional contribution to the photoexcited response, good agreement between the simulations (Figure 4b) and the experimental results (Figure 4a) is obtained. This enables calculation of the SMMA absorption for different optical pump fluences based on the parameters used in the simulations, as shown in Figure 4c. The absorption from 1.1 to 1.6 THz monotonically decreases as the pump fluence increases with the peak shifting to ∼1.0 THz with an amplitude of 0.8 at 1.5 THz, as shown in Figure 4d. This corresponds to an amplitude modulation of ∼20% between 1.4−1.6 THz with optical excitation. Furthermore, the bandwidth is maintained at 500−600 GHz even when the pump fluence is increased to 100 μJ/cm^2.

CONCLUSION

We have designed, fabricated, and characterized a broadband terahertz silicon membrane metasurface absorber exhibiting an absorption ≥90% between 1.1 and 1.6 THz at normal incidence. Utilizing effective medium theory and mode analysis, we identified the TE and TM mode contributions to the broadband absorption. Under optical pump excitation, a 20% modulation of the absorption amplitude was achieved when the optical fluence reached 1020 μJ/cm^2. The dynamic response revealed the importance of the sidewall excitation as well as the top layer excitation in this hole-based array structure due to the diffraction of the optical pump on the edge of the holes. As our silicon absorber structure is based on a thin (75 μm) layer of silicon, it is of potential interest for applications in CMOS-compatible and miniaturized devices operating at terahertz frequencies. The Si membrane we designed gives the interesting possibility of being incorporated with material systems to realize strong light-matter coupling. The thin membrane increases the ability to integrate with other materials, and can offer local field enhancement, well-defined electromagnetic modes, and increased transmission/reflection modulation.

EXPERIMENTAL SECTION

Simulation. A time domain solver (CST microwave studio) was employed for simulating the transmission and reflection of the silicon membrane metasurface. For the simulations, periodic boundary conditions were used with waveguide ports. A plane wave source with the polarization direction along the short radius of the elliptical holes was employed. The doped silicon is modeled as a Drude response with ε = 11.68, plasma frequency ω_p = 1.9 × 10^{13} Hz, and a collision frequency of γ = 6.79 × 10^{12} Hz. The plasma frequency is given by $\sqrt{n_d e^2/(\varepsilon m^*)}$, where n_d is the carrier density, e is the unit electron charge, and m^* is the effective mass of the carriers in silicon ($m^* = 0.26m_0$ is this case for n-type silicon). The collision frequency Γ is given by $\Gamma = e/(\mu m^*)$, where μ is the mobility of the carriers. In this case, the resistivity of this n-type silicon is 0.2 Ω·cm, which corresponds to a carrier density of 3 × 10^{16} cm^{-3}. Our prior work has shown that the above Drude model is accurate for the THz electromagnetic response.[42]

Fabrication. The silicon membrane metasurface was fabricated using a commercially available n-doped silicon-on-insulator (SOI) wafer with a 75 μm thick Si layer, using conventional photolithography and deep reactive ion etching (DRIE) based on large-scale microfabrication. First, a 5 μm thick layer of photoresist (AZ 9260, Microchemicals GmbH) was spin coated on top of the device layer prior to photolithography (MA6, Suss Microtec Group) to pattern the structure. Then, DRIE was used to etch through the device layer with the desired pattern. After the front etching of the SOI wafer, a 10 μm thick layer of the same photoresist was spin coated on top of the handle layer and DRIE was used again for fully removing the silicon below the insulating layer. After that, the insulating layer of 1 μm thick silicon dioxide was removed using reactive ion etching (RIE). The DRIE process was implemented using SF_6 as the etching gas and CF_4 as the passivation gas. In order to etch through the device layer, 2 turns with each turn of 50 cycles are used. Each cycle lasts for 12 s with 8 s etching and 4 s for passivation. The wafer was finally cleaned in acetone for removal of photoresist. The size of each sample is 1.2× 1.2 cm^2 with pattern size of 0.5 × 0.5 cm^2, consisting of 900 unit cells. The fabrication flow for this design is also included in the Supporting Information.

Characterization. The transmission and reflection of the silicon membrane metasurface was characterized using THz time domain spectroscopy (THz-TDS) using photoconductive antennas for the emitter and receiver. The THz pulse is generated by 25 fs, 800 nm pulses generated at 80 MHz by a titanium sapphire laser illuminating a photoconductive antenna. The pulses were focused onto the sample using off-axis parabolic mirrors. The transmitted and reflected pulses were measured using another photoconductive antenna. For the measurements, the electric field was polarized in the x-direction, as shown in Figure 1a. The measured time-domain scan were Fourier transformed into the frequency domain to obtain the spectral response. Optical-pump terahertz-probe measurements were performed using a 1 kHz Ti:sapphire regenerative amplifier laser system. For these measurements, the generation and detection of the THz pulses utilized electro-optic techniques employing [110]-oriented ZnTe crystals. Both the 800 nm pump and THz probe were focused onto the sample at normal incidence. For all of the

https://doi.org/10.1021/acsphotonics.2c00166
ACS Photonics 2022, 9, 1150−1156

measurements, the experiments were performed in a dry air chamber in order to avoid THz absorption by water vapor.

■ ASSOCIATED CONTENT

Supporting Information

The Supporting Information is available free of charge at https://pubs.acs.org/doi/10.1021/acsphotonics.2c00166.

Dielectric properties of the silicon and the comparison of the absorption spectra between the bare silicon and the proposed silicon membrane metasurface; the fabrication flow of the silicon membrane metasurface; the simulated absorption spectra with varied incidence angles; the analysis of whether sidewall excitation is included under the optical pump (PDF)

■ AUTHOR INFORMATION

Corresponding Authors

Richard D. Averitt − *Department of Physics, University of California, San Diego, La Jolla, California 92903, United States*; Email: raveritt@ucsd.edu

Xin Zhang − *Department of Mechanical Engineering and Division of Materials Science and Engineering, Boston University, Boston, Massachusetts 02215, United States*; orcid.org/0000-0002-4413-5084; Email: xinz@bu.edu

Authors

Yuwei Huang − *Department of Mechanical Engineering and Division of Materials Science and Engineering, Boston University, Boston, Massachusetts 02215, United States*

Kelson Kaj − *Department of Physics, University of California, San Diego, La Jolla, California 92903, United States*

Chunxu Chen − *Department of Mechanical Engineering and Division of Materials Science and Engineering, Boston University, Boston, Massachusetts 02215, United States*

Zhiwei Yang − *Department of Mechanical Engineering and Division of Materials Science and Engineering, Boston University, Boston, Massachusetts 02215, United States*

Sheikh Rubaiat Ul Haque − *Department of Physics, University of California, San Diego, La Jolla, California 92903, United States*

Yuan Zhang − *Department of Physics, University of California, San Diego, La Jolla, California 92903, United States*

Xiaoguang Zhao − *Department of Mechanical Engineering and Division of Materials Science and Engineering, Boston University, Boston, Massachusetts 02215, United States*

Complete contact information is available at: https://pubs.acs.org/10.1021/acsphotonics.2c00166

Funding

This work was supported by National Science Foundation ECCS-1810252. Work at UCSD was supported by DARPA Driven Nonequilibrium Quantum Systems (DRINQS) program under Award No. D18AC00014 and the Army Research Office (ARO) under Grant No. MURI W911NF-16-1-0361.

Notes

The authors declare no competing financial interest.

■ ACKNOWLEDGMENTS

We gratefully acknowledge technical support for device fabrication from Photonics Center, Boston University.

■ REFERENCES

(1) Tonouchi, M. Cutting-edge Terahertz Technology. *Nat. Photonics* **2007**, *1*, 97−105.

(2) Zhang, X. C.; Shkurinov, A.; Zhang, Y. Extreme Terahertz Science. *Nat. Photonics* **2017**, *11*, 16−18.

(3) Nagatsuma, T.; Ducournau, G.; Renaud, C. C. Advances in Terahertz Communications Accelerated by Photonics. *Nat. Photonics* **2016**, *10*, 371−379.

(4) Zheludev, N. I.; Kivshar, Y. S. From Metamaterials to Metadevices. *Nat. Mater.* **2012**, *11*, 917−924.

(5) Yu, N.; Capasso, F. Flat Optics with Designer Metasurfaces. *Nat. Mater.* **2014**, *13*, 139−150.

(6) Estakhri, N. M.; Alu, A. Wave-front Transformation with Gradient Metasurfaces. *Phys. Rev. X* **2016**, *6*, 041008.

(7) Chen, H.-T.; Padilla, W. J.; Cich, M. J.; Azad, A. K.; Averitt, R. D.; Taylor, A. J. A Metamaterial Solid-state Terahertz Phase Modulator. *Nat. Photonics* **2009**, *3*, 148−151.

(8) Shrestha, S.; Wang, Y.; Overvig, A. C.; Lu, M.; Stein, A.; Negro, L. D.; Yu, N. Indium Tin Oxide Broadband Metasurface Absorber. *ACS Photonics* **2018**, *5*, 3526−3533.

(9) Chen, C.; Huang, Y.; Wu, K.; Bifano, T. G.; Anderson, S. W.; Zhao, X.; Zhang, X. Polarization Insensitive, Metamaterial Absorber-enhanced Long-wave Infrared Detector. *Opt. Express* **2020**, *28*, 28843−28857.

(10) Arbabi, A.; Arbabi, E.; Horie, Y.; Kamali, S. M.; Faraon, A. Planar Metasurface Retroreflector. *Nat. Photonics* **2017**, *11*, 415−420.

(11) Chen, C.; Kaj, K.; Zhao, X.; Huang, Y.; Averitt, R. D.; Zhang, X. On-demand Terahertz Surface Wave Generation with Micro-electromechanical-system-based Metasurface. *Optica* **2022**, *9*, 17−25.

(12) Liu, X.; Bi, K.; Li, B.; Zhao, Q.; Zhou, J. Metamaterial Perfect Absorber Based on Artificial Dielectric "atoms. *Opt. Express* **2016**, *24*, 20454−20460.

(13) Liu, C.; Yang, L.; Lu, X.; Liu, Q.; Wang, F.; Lv, J.; Sun, T.; Mu, H.; Chu, P. K. Mid-infrared Surface Plasmon Resonance Sensor Based on Photonic Crystal Fibers. *Opt. Express* **2017**, *25*, 14227−14237.

(14) Akselrod, G. M.; Huang, J.; Hoang, T. B.; Bowen, P. T.; Su, L.; Smith, D. R.; Mikkelsen, M. H. Metasurfaces: Large-Area Metasurface Perfect Absorbers from Visible to Near-Infrared (Adv. Mater. 48/2015). *Adv. Mater.* **2015**, *27*, 7897.

(15) Yu, W.; Lu, Y.; Chen, X.; Xu, H.; Shao, J.; Chen, X.; Sun, Y.; Hao, J.; Dai, N. Large-Area, Broadband, Wide-Angle Plasmonic Metasurface Absorber for Midwavelength Infrared Atmospheric Transparency Window. *Adv. Opt. Mater.* **2019**, *7*, 1900841.

(16) Cheng, Y.; Zhao, H.; Li, C. Broadband Tunable Terahertz Metasurface Absorber Based on Complementary-wheel-shaped Graphene. *Opt. Mater.* **2020**, *109*, 110369.

(17) Cheng, Y.; Liu, J.; Chen, F.; Luo, H.; Li, X. Optically Switchable Broadband Metasurface Absorber Based on Square Ring Shaped Photoconductive Silicon for Terahertz Waves. *Phys. Lett. A* **2021**, *402*, 127345.

(18) Cheng, Y.; Li, Z.; Cheng, Z. Terahertz Perfect Absorber Based on InSb Metasurface for Both Temperature and Refractive Index Sensing. *Opt. Mater.* **2021**, *117*, 111129.

(19) Li, W.; Cheng, Y. Dual-band Tunable Terahertz Perfect Metamaterial Absorber Based on Strontium Titanate (STO) Resonator Structure. *Opt. Commun.* **2020**, *462*, 125265.

(20) Li, A.; Zhao, X.; Duan, G.; Anderson, S.; Zhang, X. Metamaterials: Diatom Frustule-Inspired Metamaterial Absorbers: The Effect of Hierarchical Pattern Arrays (Adv. Funct. Mater. 22/2019). *Adv. Funct. Mater.* **2019**, *29*, 1970151.

(21) Tao, H.; Landy, N. I.; Bingham, C. M.; Zhang, X.; Averitt, R. D.; Padilla, W. J. A Metamaterial Absorber for the Terahertz Regime: Design, Fabrication and Characterization. *Opt. Express* **2008**, *16*, 7181−7188.

(22) Chen, C.; Can, S.; Schalch, J.; Zhao, X.; Duan, G.; Averitt, R. D.; Zhang, X. Ultrathin Terahertz Triple-Band Metamaterial Absorbers: Consideration of Interlayer Coupling. *Phys. Rev. Appl.* **2020**, *14*, 054021.

(23) Zhu, H.; Yi, F.; Cubukcu, E. Plasmonic Metamaterial Absorber for Broadband Manipulation of Mechanical Resonances. *Nat. Photonics* **2016**, *10*, 709−714.
(24) Fan, K.; Suen, J. Y.; Liu, X.; Padilla, W. J. All-dielectric Metasurface Absorbers for Uncooled Terahertz Imaging. *Optica* **2017**, *4*, 601−604.
(25) Cardin, A.; Fan, K.; Padilla, W. Role of Loss in All-dielectric Metasurfaces. *Opt. Express* **2018**, *26*, 17669−17679.
(26) Yang, Y.; Kravchenko, I. I.; Briggs, D. P.; Valentine, J. All-dielectric Metasurface Analogue of Electromagnetically Induced Transparency. *Nat. Commun.* **2014**, *5*, 1−7.
(27) Ma, T.; Huang, Q.; He, H.; Zhao, Y.; Lin, X.; Lu, Y. All-dielectric Metamaterial Analogue of Electromagnetically Induced Transparency and Its Sensing Application in Terahertz Range. *Opt. Express* **2019**, *27*, 16624−16634.
(28) Sun, G.; Peng, S.; Zhang, X.; Zhu, Y. Switchable Electromagnetically Induced Transparency with Toroidal Mode in a Graphene-loaded All-dielectric Metasurface. *Nanomaterials* **2020**, *10*, 1064.
(29) Han, S.; Pitchappa, P.; Wang, W.; Srivastava, Y. K.; Rybin, M. V.; Singh, R. Extended Bound States in the Continuum with Symmetry-Broken Terahertz Dielectric Metasurfaces. *Adv. Opt. Mater.* **2021**, *9*, 2002001.
(30) Han, S.; Cong, L.; Srivastava, Y. K.; Qiang, B.; Rybin, M. V.; Kumar, A.; Jain, R.; Lim, W. X.; Achanta, V. G.; Prabhu, S. S.; et al. All-Dielectric Active Terahertz Photonics Driven by Bound States in the Continuum. *Adv. Mater.* **2019**, *31*, 1901921.
(31) Tuz, V. R.; Khardikov, V. V.; Kivshar, Y. S. All-dielectric Resonant Metasurfaces with a Strong Toroidal Response. *ACS Photonics* **2018**, *5*, 1871−1876.
(32) He, Y.; Guo, G.; Feng, T.; Xu, Y.; Miroshnichenko, A. E. Toroidal Dipole Bound States in the Continuum. *Phys. Rev. B* **2018**, *98*, 161112.
(33) Lin, D.; Fan, P.; Hasman, E.; Brongersma, M. L. Dielectric Gradient Metasurface Optical Elements. *Science* **2014**, *345*, 298−302.
(34) Decker, M.; Staude, I.; Falkner, M.; Dominguez, J.; Neshev, D. N.; Brener, I.; Pertsch, T.; Kivshar, Y. S. High-efficiency Dielectric Huygens' Surfaces. *Adv. Opt. Mater.* **2015**, *3*, 813−820.
(35) Yang, Q.; Liu, M.; Kruk, S.; Xu, Y.; Srivastava, Y. K.; Singh, R.; Han, J.; Kivshar, Y.; Shadrivov, I. V. Polarization-Sensitive Dielectric Membrane Metasurfaces. *Adv. Opt. Mater.* **2020**, *8*, 2000555.
(36) Yang, Q.; Kruk, S.; Xu, Y.; Wang, Q.; Srivastava, Y. K.; Koshelev, K.; Kravchenko, I.; Singh, R.; Han, J.; Kivshar, Y.; et al. Mie-resonant Membrane Huygens' Metasurfaces. *Adv. Funct. Mater.* **2020**, *30*, 1906851.
(37) Ong, J. R.; Chu, H. S.; Chen, V. H.; Zhu, A. Y.; Genevet, P. Freestanding Dielectric Nanohole Array Metasurface for Mid-infrared Wavelength Applications. *Opt. Lett.* **2017**, *42*, 2639−2642.
(38) Haerinia, M.; Fowler, C.; An, S.; Tang, H.; Zheng, B.; Dong, Y.; Guo, W.; Zhang, H. *Design of Ultra-thin Near-infrared Freestanding Dielectric Meta-optics Devices*; International Applied Computational Electromagnetics Society Symposium (ACES), 2021; pp 1−4.
(39) Zhao, Q.; Zhou, J.; Zhang, F.; Lippens, D. Mie Resonance-based Dielectric Metamaterials. *Mater. Today* **2009**, *12*, 60−69.
(40) Liu, Y.; Liu, Q.; Li, Y.; Xu, B.; Zhang, J.; He, Z. High-resolution Multi-wavelength Lensless Diffraction Imaging with Adaptive Dispersion Correction. *Opt. Express* **2021**, *29*, 7197−7209.
(41) Wu, S.; Ye, Y.; Jiang, Z.; Yang, T.; Chen, L. Large-Area, Ultrathin Metasurface Exhibiting Strong Unpolarized Ultrabroadband Absorption. *Adv. Opt. Mater.* **2019**, *7*, 1901162.
(42) Zhao, X.; Wang, Y.; Schalch, J.; Duan, G.; Cremin, K.; Zhang, J.; Chen, C.; Averitt, R. D.; Zhang, X. Optically Modulated Ultra-broadband All-silicon Metamaterial Terahertz Absorbers. *ACS Photonics* **2019**, *6*, 830−837.
(43) Smith, D.; Vier, D.; Koschny, T.; Soukoulis, C. Electromagnetic Parameter Retrieval From Inhomogeneous Metamaterials. *Phys. Rev. E* **2005**, *71*, 036617.
(44) Smith, D.; Schultz, S.; Markoš, P.; Soukoulis, C. Determination of Effective Permittivity and Permeability of Metamaterials from Reflection and Transmission Coefficients. *Phys. Rev. B* **2002**, *65*, 195104.
(45) Fan, K.; Shadrivov, I. V.; Padilla, W. J. Dynamic Bound States in the Continuum. *Optica* **2019**, *6*, 169−173.

https://doi.org/10.1021/acsphotonics.2c00166
ACS Photonics 2022, 9, 1150−1156